

The Heavy Photon Search Test Detector

C. Field^a, P. Hansson Adrian^a, N. Graf^a, M. Graham^a, G. Haller^a, R. Herbst^a, J. Jaros^a, T. Maruyama^a, J. McCormick^a, K. Moffeit^a, T. Nelson^a, H. Neal^a, A. Odian^a, M. Oriunno^a, S. Uemura^a, D. Walz^a, A. Grillo^b, V. Fadeyev^b, O. Moreno^b, W. Cooper^c, S. Boyarinov^d, V. Burkert^d, A. Deur^d, H. Egiyan^d, L. Elouadrhiri^d, A. Freyberger^d, F.-X. Girod^d, V. Kubarovskiy^d, Y. Sharabian^d, S. Stepanyan^d, M. Ungaro^d, B. Wojtsekhowski^d, R. Essig^e, M. Holtrop^f, K. Slifer^f, S. K. Phillips^f, A. Fradi^g, B. Guegan^g, M. Guidal^g, S. Niccolai^g, S. Pisano^g, E. Rauly^g, P. Rosier and D. Sokhan^g, P. Schuster^h, N. Toro^h, N. Dashyanⁱ, N. Gevorgyanⁱ, R. Paremuzyanⁱ, H. Voskanyanⁱ, M. Khandaker^j, C. Salgado^j, M. Battaglieri^k, R. De Vita^k, S. Bueltmann^l, L. Weinstein^l, P. Stoler^m, A. Kubarovskiy^m, K. Griffioenⁿ

^aSLAC National Accelerator Laboratory, Menlo Park, CA 94025

^bUniversity of California, Santa Cruz, CA 95064

^cFermi National Accelerator Laboratory, Batavia, IL 60510-5011

^dThomas Jefferson National Accelerator Facility, Newport News, Virginia 23606

^eStony Brook University, Stony Brook, NY 11794-3800

^fUniversity of New Hampshire, Department of Physics, Durham, NH 03824

^gInstitut de Physique Nucléaire d'Orsay, IN2P3, BP 1, 91406 Orsay, France

^hPerimeter Institute, Ontario, Canada N2L 2Y5

ⁱYerevan Physics Institute, 375036 Yerevan, Armenia

^jNorfolk State University, Norfolk, Virginia 23504

^kIstituto Nazionale di Fisica Nucleare, Sezione di Genova e Dipartimento di Fisica dell'Università, 16146 Genova, Italy

^lOld Dominion University, Norfolk, Virginia 23529

^mRensselaer Polytechnic Institute, Department of Physics, Troy, NY 12181

ⁿThe College of William and Mary, Department of Physics, Williamsburg, VA 23185

Abstract

Construction and design of the Heavy Photon Search (HPS) experiment, designed to search for an e^+e^- resonance from heavy photon production in a fixed-target setup at the Thomas Jefferson Accelerator Facility (JLab), is ongoing. As a first stage, a test apparatus was constructed and operated at JLab to demonstrate that the apparatus and data acquisition systems are technically feasible and that the trigger rates and occupancies encountered in electron-beam running are as simulated. Given dedicated running time with electron beams, the HPS Test apparatus is capable of searching for heavy photons in unexplored regions of parameter space. Charged particle tracks are measured with a compact forward silicon microstrip detector and electromagnetic showers from electrons and photons are detected in a dense array of PbWO₄ crystals. To allow clean passage of the scattered intense electron beam after the thin tungsten target foil while keeping sensitivity to low-mass heavy photons, the sensitive region of the detectors are placed at ± 15 mrad with respect to the horizontal beam plane. The discrimination between prompt and displaced e^+e^- pairs requires the first layer of silicon sensors to be placed only 10 cm behind the target and 0.5 mm from the beam. The HPS Test apparatus included the high-speed trigger and data acquisition needed for running with electron beams. Details of the layout and performance of the Test detectors and associated readout electronics are presented.

Keywords: silicon microstrip, tracking, vertexing, heavy photon, dark photon, hidden sector, electromagnetic calorimeter

*Corresponding author

Email address: phansson@slac.stanford.edu (P. Hansson Adrian)

Contents

1	Introduction	3
2	Detector Overview	3
3	The HPS Test Run Beamline	4
4	Silicon Vertex Tracker	5
4.1	Layout	6
4.2	Components	6
4.3	Production, Assembly and Shipping . .	7
4.4	Alignment	7
5	Electromagnetic Calorimeter	8
5.1	Components	8
5.2	Layout	8
5.3	Signal readout	8
6	Trigger and Data Acquisition	9
6.1	Trigger system	9
6.2	SVT Data Acquisition	10
6.3	General Data Acquisition and Online Computing	11
7	Performance	11
7.1	SVT Performance	11
7.1.1	Cluster and Hit Reconstruction .	11
7.1.2	Momentum and Vertexing Resolution	12
7.2	ECal Performance	13
7.3	Trigger Performance	13
8	Multiple Coulomb Scattering Distributions	15
8.1	Multiple Coulomb Scattering Models .	15
8.2	Running Conditions	15
8.3	Measured Angular Distributions	15
8.4	Conclusion	16
9	Summary and Outlook	17
10	Acknowledgements	17

1. Introduction

Heavy photons, aka "hidden sector" or "dark" photons, or from here on A', are particles with mass 10 – 1000 MeV which couple weakly to the Standard Model photon [1], so can be radiated by electrons, and can decay into e^+e^- -pairs, albeit at rates far below those of QED trident processes. They have been suggested by numerous Beyond Standard Model theories and as an explanation of the current muonic $g - 2$ anomaly, and may couple directly to hidden sector particles that may constitute all or some of the dark matter [2]. Current phenomenology highlights the 20 – 1000 MeV/c² mass range, and suggests that A' s couple to electric charge with strength ϵe , where ϵ is in the range of $10^{-3} - 10^{-5}$. [REFERENCE]. This range of parameters makes A' searches viable in moderate energy fixed target electroproduction [3], but require large data sets and good mass resolution to identify a small mass peak above the copious QED background at very small production angles. At small couplings, A' s become long-lived, so detection of a displaced decay vertex can reject the prompt QED background and boost experimental sensitivity. These production and kinematics poses stringent constraint on the detector requirements:

- large and uniform acceptance in the forward region close to the beam in order to catch boosted A' decay products,
- beam passage through the apparatus in vacuum, to eliminate direct interactions with the detector and minimize beam gas interactions,
- a flexible, redundant and efficient trigger selecting electron and positron pairs at rates up to 50 kHz,
- excellent track reconstruction efficiency for electrons and positrons,
- good angular and momentum resolution to reconstruct invariant mass precisely,
- excellent vertex resolution to discriminate displaced A' decays from prompt QED backgrounds,
- high rate electronics with excellent timing resolution to minimize out of time backgrounds,
- data handling rates of 100 MB/s to permanent storage,
- detector components that can survive and efficiently operate in a high radiation environment with local doses exceeding 100 Mrad.

The HPS experiment [4] uses both invariant mass and vertex signatures by placing a ≈ 1 m long silicon tracking and vertexing detector 10 cm downstream of a 0.25% χ_0 tungsten target inside a dipole magnet. The experiment runs at high rates (up to 50kHz), exploiting the 100% duty cycle of the Thomas Jefferson National Accelerator Facility (JLab) CEBAF accelerator to accumulate the need statistics. The trigger is provided by a fast electromagnetic calorimeter just downstream of the tracking detector.

The HPS Test apparatus, a simplified version of the full HPS experiment, was proposed and approved at Thomas Jefferson National Accelerator Facility (JLab) as the first stage of the HPS experiment. Its purposes included demonstrating that the apparatus and data acquisition systems are technically feasible and that the trigger rates and occupancies encountered in electron-beam running are as simulated. Given dedicated running time with electron beams, the HPS Test Run apparatus is capable of searching for heavy photons in unexplored regions of parameter space. The HPS Test apparatus was installed on April 19, 2012, and ran parasitically with the HDice experiment [5], using its photon beam, until May 18. The JLab run schedule precluded any dedicated electron beam running, but the HPS Test Run was allowed a short and valuable dedicated run with the photon beam. Most technologies used in the Test apparatus will be used in the HPS detector with some improvements to each of the systems; both from lessons learned during running of the Test run but also from less schedule and budget constraints.

This paper reviews the HPS Test Run apparatus; documents the performance of the trigger, data acquisition, silicon tracking detector, and the electromagnetic calorimeter at the level assumed in calculating the physics reach of the HPS experiment.

2. Detector Overview

The HPS Test apparatus was designed to run in Hall B at JLab using the CEBAF electron beam, a 499 MHz beam, at an energy of 2.2 and 6.6 GeV and currents between 200 and 600 nA. The overall design of the experiment follows from the kinematics of A' production which typically results in final state particles within a few degrees of the incoming beam, especially at low $m_{A'}$. Detectors must therefore be placed close to the beam. The intense electron beam and the degraded electrons after the target are spread out horizontally by the analyzing magnet constitute a "dead zone" which must

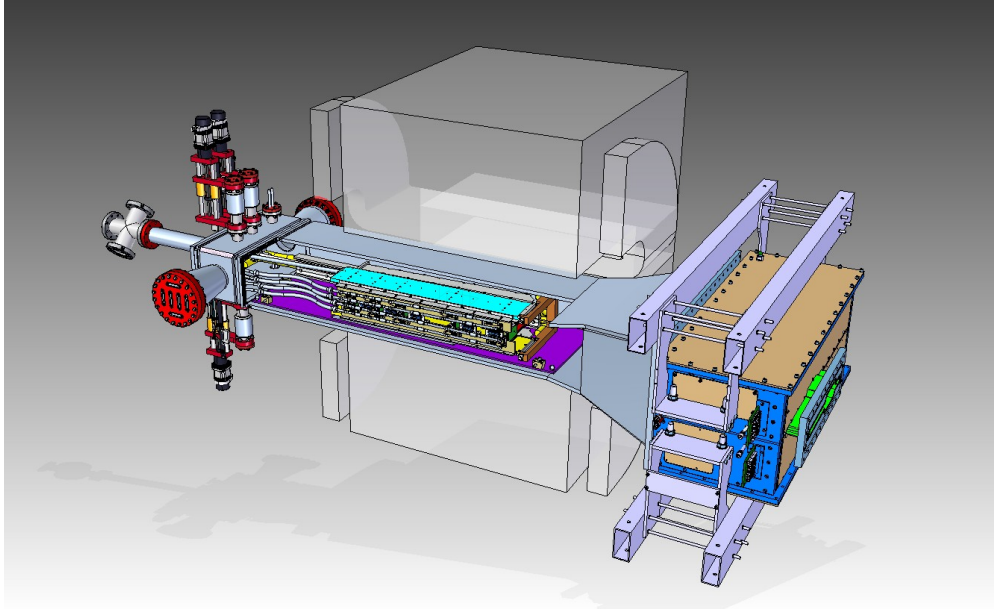


Figure 1: Rendering of the HPS Test apparatus installed on the beam line.

be completely avoided. The apparatus is split vertically 15 mrad above and below the beam plane and the beam is transported in vacuum to minimize beam-gas interaction backgrounds. Even so, background occupancy in the detectors remain high and are dominated by the degraded primary beam, so high rate detectors, a fast trigger, and excellent time tagging are required to minimize their impact. At masses below $2m_\mu$ only decays to electrons are allowed, so the key trigger comes from a PbWO₄ crystal calorimeter.

A rendering of the HPS Test apparatus installed on the beam line is shown in Fig. 1 and an overview of the coverage, segmentation and performance is given in Tab. 1.

The silicon tracking and vertexing detector for HPS Test, or SVT, operates in an existing vacuum chamber inside the pair spectrometer analyzing magnet in Hall B at JLab. There are five measurement stations, or “layers,” placed immediately downstream of the target. Each layer comprises a pair of closely-spaced silicon microstrip sensors responsible for measuring a single coordinate, or “view.” Introduction of a small (50 or 100 mrad) stereo angle between the two sensors of each layer provides three-dimensional tracking and vertexing throughout the acceptance of the detector with one redundant layer. Each layer In order to accommodate the dead zone, the SVT is built in two halves that are mirror reflections of one another about the plane of the nominal

electron beam. Each layer in one half are supported on a common support plate with independent cooling and readout.

Each half of the electromagnetic calorimeter, or ECal, consists of 221 PbWO₄ crystals arranged in rectangular formation. There are five rows with 46 modules in each row except the row closest to the beam plane which has 37. The light from each crystal is read out by Avalanche Photodiode (APD) glued on the back surface of the crystal. Signals from the APDs were amplified using custom-made amplifier boards before being sent to the readout electronics.

The Data Acquisition system combines two architectures, the Advanced Telecom Communications Architecture (ATCA) based SVT readout system and VXS based digitization and triggering system for the ECal. The system was designed to run at up to 20 kHz trigger rate.

3. The HPS Test Run Beamline

The HPS Test run studied multiple Coulomb scattering of electrons and positrons from bremsstrahlung photons produced in the Hall B tagged photon facility. Figure 2 shows the layout of the HPS Test setup on the beam line. The SVT was installed inside the Hall B pair spectrometer magnet (PS) vacuum chamber with the ECal mounted downstream of it. Both the SVT and the ECal were retracted off the beam plane compared to

Table 1: Overview of the coverage, segmentation and performance of the HPS Test detector.

System	Coverage (mrad)	# channels	ADC (bit)	Time resolution (ns)	# layers	Segmentation	Performance
SVT	$15 < \theta_y < XXXX$	12800	14	≈ 2 ns	5 (stereo layers)	$\approx 120 \mu\text{m} r - \phi$ $\approx 6 \mu\text{m} z$	$\sigma_{d0,y} \approx 100 \mu\text{m}$ $\sigma_{d0,x} \approx 300 \mu\text{m}$ $\sigma_{d0,z} \approx 1 \text{ mm}$
Ecal	$15 < \theta_y < XXXX$	442	12	4 ns	1	$1.3 \times 1.3 \text{ cm}^2$ $1.6 \times 1.6 \text{ cm}^2$	$\sigma(E)/E \approx 4.5\%$

nominal electron beam running to allow clean passage of the photon beam through the system.

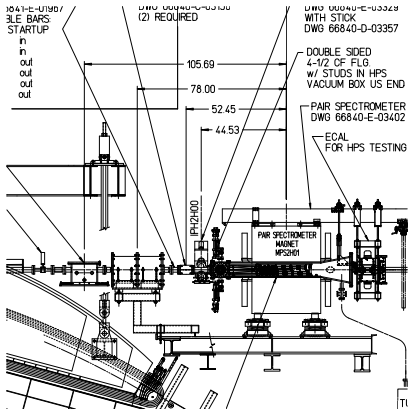


Figure 2: Layout of the HPS parasitic run.

The photon beam was generated in the interaction of 5.5 GeV electrons with a $10^{-4} X_0$ gold radiator located ≈ 9 m upstream of the PS. The primary beam and scattered electrons are deflected away from detectors by the dipole magnet of the photon tagging system. During the dedicated HPS Test run period, the collimated (6.4 mm diameter), photon beam passes through the aluminum PS pair converter and later the HPS system as shown schematically in Fig. 3. The PS pair converter was located ≈ 77 cm upstream of the first layer of the SVT. Data was taken on different converters (empty, $1.8 \times 10^{-3} X_0$, $4.5 \times 10^{-3} X_0$ and $1.6 \times 10^{-2} X_0$) and repeated with the reverse field setting of the PS dipole magnet.

4. Silicon Vertex Tracker

The Silicon Vertex Tracker (SVT) enables efficient reconstruction of charged particles and precision determination of their trajectories. These measurements allow A' decays to be distinguished from background via simultaneous estimation of the invariant mass of e^+e^- decay products and the position of decay vertexes downstream of the target.

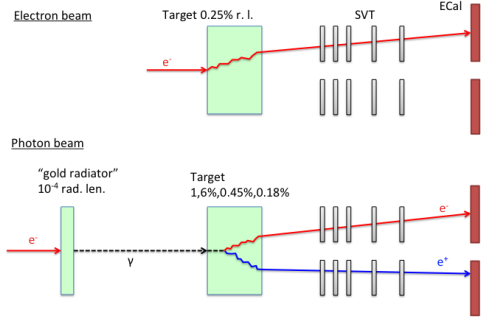


Figure 3: Schematic comparison of HPS Test run photon beam compared to the HPS electron beam.

The design of the SVT is primarily driven by direct physics requirement and constraints from the environment at the interaction region. The A' decay products have momenta in the range of 1 GeV, so multiple scattering dominates mass and vertexing uncertainties for any possible material budget, so the SVT must minimize the amount of material in the tracking volume. The signal yield for long-lived A' 's is very small, so the rejection of prompt vertexes must be exceedingly pure, on the order of 10^{-7} , in order to eliminate all prompt backgrounds. To achieve the required vertexing performance the first layer of the SVT must be placed no more than about 10 cm downstream of the target. At that distance, it is found that the active region of a sensor can be placed as close to 1.5 mm from the center of the beam, defining the 15 mrad “dead zone” mentioned previously, to maximize low-mass A' acceptance with decay products nearly collinear with the beam axis. At the edge of this “dead zone,” the radiation dose approaches 10^{15} electrons/cm 2 /month, or roughly 3×10^{14} 1 MeV neutron equivalent/cm 2 /month [7], as shown in Fig. 4, requiring the sensors to be actively cooled. Meanwhile, very low-energy delta rays from beam-gas interactions multiply the density of background hits, so the SVT must operate inside the beam vacuum. Finally, in or-

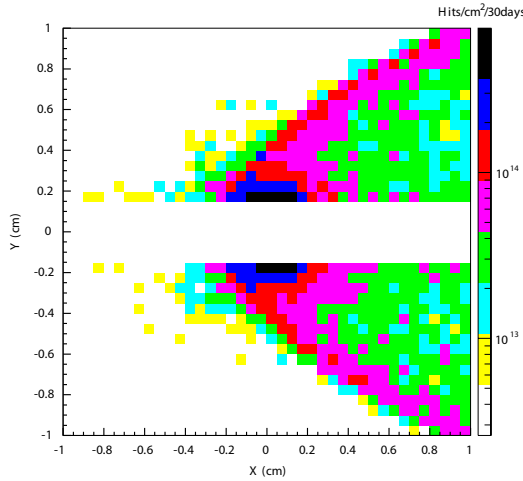


Figure 4: Simulation of the electron fluence 10 cm downstream of the target in the active region of the SVT ($|Y| > 0.15$ mm) looking downstream; electrons bend towards $+x$.

der to protect the sensors, the detector must be movable so that it can be retracted during periods of uncertain beam conditions.

4.1. Layout

The layout of the SVT is summarized in Tab. 4.1 and rendered in Fig. 5. Each of the layers is comprised of a pair of closely-spaced silicon microstrip sensors mounted back-to-back to form a module. A 100 mrad stereo angle is used in the first three layers to provide higher-resolution 3D space points for vertexing. Using 50 mrad in the last two layers breaks the tracking degeneracy of having five identical layers and minimizes fakes from ghost hits to improve pattern recognition. Altogether, the SVT comprises 20 sensors for a total of 12780 readout channels.

Layer	1	2	3	4	5
z from target (cm)	10	20	30	50	70
Stereo angle (mrad)	100	100	100	50	50
Bend res. (μm)	≈ 60	≈ 60	≈ 60	≈ 120	≈ 120
Non-bend res. (μm)	≈ 6	≈ 6	≈ 6	≈ 6	≈ 6
# of sensors	4	4	4	4	4
Dead zone (mm)	± 1.5	± 3.0	± 4.5	± 7.5	± 10.5
Power cons. (W)	6.9	6.9	6.9	6.9	6.9

Table 2: Layout of the SVT.

The SVT is built in two separate halves that are mirror reflections of one another about the plane of the nominal electron beam. Each half consists of five modules mounted on a support plate that provides services to the

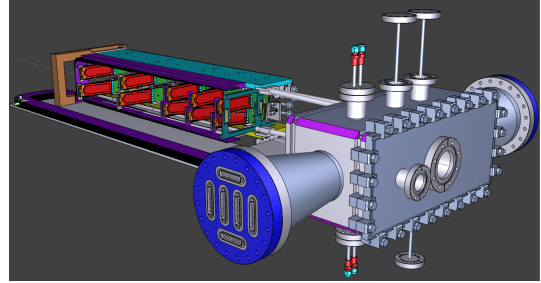


Figure 5: A rendering of the SVT showing the modules on their support plates held by the hinged C-support on the left and the motion levers on the right. The sensors are shown in red and the hybrid readout boards in green. The beam enters from the right through a vacuum box with flanges for services.

modules and allows them to be moved as a group relative to the dead zone. The two halves of the tracker are connected to hinges mounted on a C-shaped support just beyond the last layer that defines the nominal spacing between the upper and lower halves of the tracker. A shaft attached to each support plate in front of layer 1 extends upstream and connects to a linear shift that transfers motion into the vacuum box through bellows to open and close the two halves around the dead zone. The C-support is mounted to an aluminum baseplate that defines the position of the SVT with respect to the vacuum chamber. Figure 6 shows a photograph of both completed detector halves prior to final assembly.



Figure 6: Both halves of the HPS Test SVT after final assembly at SLAC. The cooling manifolds and integrated cable runs are clearly seen.

4.2. Components

The sensors for the SVT are $p+$ -on- n , single sided, AC coupled, polysilicon-biased microstrip sensors fabricated on $< 100 >$ silicon and have 30 (60) micron

sense (readout) pitch over their $4 \times 10 \text{ cm}^2$ surface. This sensor technology was selected to match the requirement of a $< 1\% X_0$ per layer, single-hit resolution better than $50 \mu\text{m}$ and tolerant of a radiation dose of approximately $1.5 \times 10^{14} 1 \text{ MeV}$ neutron equivalent/ cm^2 for a six month run. The sensors were purchased from the Hamamatsu Photonics Corporation for the cancelled Run 2b upgrade of the DØ experiment [10] which satisfied the requirement that the technology must be mature and available within the time and budget constraints.

Despite having only small spots with very high occupancy (up to 4 MHz/mm^2) closest to the primary beam, see Fig. 4, the rates are still high and lowering the peak occupancy to approximately 1% for tracking requires a trigger window and hit time tagging of roughly 8 ns. The ECal readout and trigger described in Sec. 5.3 can achieve such resolution. To reach this performance the sensors for the SVT are readout by the APV25 ASIC developed for the CMS experiment at CERN [11]. The APV25 can capture two successive samples of three of the output of the shaper at a sampling rate of approximately 40 MHz. By fitting the known *CR-RC* shaping curve to these samples, the initial time of the hit can be determined to a precision of 2 ns for $S/N \approx 25$ [12]. For electron beam running, six-sample readout and the shortest possible shaping time (35 ns) is used to best distinguish hits that overlap in time. The APV25 ASICs are hosted on simple FR4 hybrid readout boards, outside the tracking volume, with a short twisted-pair pigtail cable to provide power and configuration and signal readout. Along with a single sensor, these are glued to a polyamide-laminated carbon fiber composite backing making up a half-module. A window is machined in the carbon fiber leaving only a frame around the periphery of the silicon to minimize material. A $50 \mu\text{m}$ sheet of polyamide is laminated to the surface of the carbon fiber with 1 mm overhang at all openings to ensure good isolation between the backside of the sensor, carrying high-voltage bias, and the carbon fiber which is held near ground.

The sensor modules for the SVT consist of a pair of identical half-modules, sandwiched back-to-back around an aluminum cooling block at one end and a similar PEEK spacer block at the other. Figure 7 shows a single module after assembly. The cooling block provides the primary mechanical support for the module as well as cooling via copper tubes pressed into grooves in the plates. The spacer block defines the spacing between the sensors at the far end of the module, stiffens the module structure, and improves the stability of the sensor alignment. The average support material in the tracking volume is approximately $0.06\% X_0$ per double-

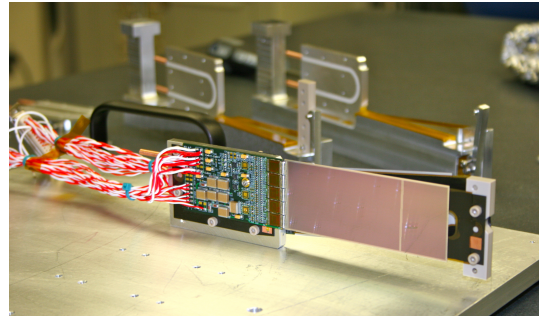


Figure 7: A prototype module assembly (foreground) with the 50 mrad (left) and 100 mrad (right) module assembly fixtures in the background. A pair of cooling blocks and a spacer block can be seen on the fixtures.

sided module for a total material budget of 0.7% per layer.

The total SVT power consumption budget of about 50 W is removed by a water/glycol mixture circulated through a flexible manifold attached to the copper tubes in the cooling blocks. During the Test run the sensors where operated at around 23°C . The power consumption is dominated by five APV25 ASICs on each hybrid board consuming approximately 2 W, radiant heat load is less than 0.5 W per sensor and leakage current is only significant in a small spot after irradiation.

4.3. Production, Assembly and Shipping

Hybrids with APV25 ASICs underwent quick qualification testing and each half-module was run at low temperature ($\approx 5^\circ\text{C}$) and fully characterized for pedestals, gains, noise and time response after assembly. Of 29 half-modules built, 28 passed qualification testing, leaving 8 spare modules after completion of the SVT, all capable of 1000 V bias voltage without breakdown. Full-module assembly and mechanical surveys were performed at SLAC before final assembly, testing and shipping of the SVT to JLab. A custom shipping container with nested crates and redundant isolation for shock and vibration was built in order to safely send the partly assembled SVT to JLab. At JLab, the entire SVT was integrated with the full DAQ and the power supplies before moving the module-loaded support plates to Hall B for final mechanical assembly and installation inside of the vacuum chamber.

4.4. Alignment

The SVT was aligned using a combination of optical, laser and touch probe surveys at SLAC and JLab. The optical survey of individual modules with precision of a few μm are combined with a touch-probe survey of

the overall SVT support structure, with 25-100 μm precision, to locate the silicon sensor layers with respect to the support plates and the mechanical survey balls on the base plate. After full assembly and installation of the SVT at JLab, a mechanical survey of the SVT base plate position inside the pair spectrometer vacuum chamber is used to determine the global position of the SVT with respect to CEBAF beam line. The resulting survey-based alignment has the position of the silicon sensors correct to within a few hundred microns measured from tracks in the Test run data. A more sophisticated global track-based alignment technique to reach final alignment precision well below 50 μm is being developed.

5. Electromagnetic Calorimeter

The electromagnetic calorimeter (ECal), installed downstream of the PS dipole magnet, performs two essential functions for the experiment: it provides a trigger signal to select what events to read out from the detector sub-systems and is used in the analysis to identify electrons and positrons. The technology and design choices are largely driven by the need for a compact forward design covering the SVT A'acceptance and able to fully absorb electrons and positrons with energy between 0.5-6.5 GeV, fine granularity and signal readout speed to handle 1 MHz/cm² of electromagnetic background and remain operable after a radiation dose larger than X MRad. The lead-tungstate (PbWO_4) crystal inner calorimeter of the CLAS detector [REFERENCE] in operation since 2005 in Hall B meet all the requirements set by HPS. The modules from this calorimeter have been subsequently repurposed for HPS.

5.1. Components

The ECal module shown in Fig. 8 is based on a tapered 160 mm long lead-tungstate (PbWO_4) crystal with a $13.3 \times 13.3 \text{ mm}^2$ ($16 \times 16 \text{ mm}^2$) front (rear) face wrapped in VM2000 multilayer polymer mirror film. The scintillation light, approximately X photoelectrons/MeV, is readout by a $5 \times 5 \text{ mm}^2$ Hamamatsu S8664-55 Avalanche Photodiode (APD) with 75% quantum efficiency glued to the rear face surface using MeltMount 1.7 thermal plastic adhesive. The low gain of APDs (~ 200) was compensated with custom made preamplifier boards, which provide factor of 2000 amplification of the APD signal.

5.2. Layout

Similar to the SVT, the ECal is built in two separate halves that are mirror reflections of one another about

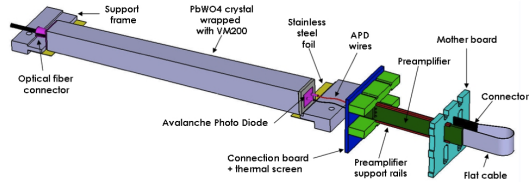


Figure 8: Schematic view of an ECal module.

the plane of the nominal electron beam to avoid interfering with the 15 mrad "dead zone". As shown in Fig. 9, the 221 modules, supported by aluminum support frames, in each half are arranged in rectangular formation with 5 layers and 46 crystals/layer except for the layer closest to the beam where 9 modules were removed to allow a larger opening for the outgoing electron and photon beams. Each half was enclosed in a temperature controlled box ($< 1^\circ \text{ F}$ stability and $< 4^\circ \text{ F}$ uniformity) to stabilize the crystal light yield and the operation of the APDs and its preamplifiers. Four printed circuit boards mounted on the backplane penetrated the enclosure and was used to supply the $\pm 5 \text{ V}$ operating voltage for the preamplifiers and the 400 V bias voltage to the APDs and to read out signals from the APDs. Each half of the ECal was divided into 12 bias voltage groups with a gain uniformity of about 20%.

During the Test run, both halves were held in place by four vertical bars attached to an above rail, placing the front face of the crystals 147 cm from the upstream edge of the magnet and with a 8.7 cm gap between the innermost edge of the crystals in the two halves.

5.3. Signal readout

After a 2:1 signal splitter, 1/3 of an amplified APD signal (2/3 is sent to a timing module) is fed to a single channel of a JLab flash ADC (FADC) board [15], see Fig. 10. The FADC boards are high speed VXS modules digitizing up to 16 APD signals at 250 MHz and storing samples in 8 μs deep pipelines with 12-bit resolution. When a trigger is received, the part of the pipeline from 5 samples before and 30 after the signal crossed a programmable threshold (for the Test run this was set to $\approx 70 \text{ MeV}$) are summed and stored in a 17-bit register for readout as described in Fig. 11. This scheme significantly compresses the data output of the FADC. During offline data analysis, a calibrated pedestal value is subtracted to obtain the actual summed energy. Two 20-slot VXS crates with 14 (13) FADC boards were employed in the Test run to read out the top (bottom) half of the

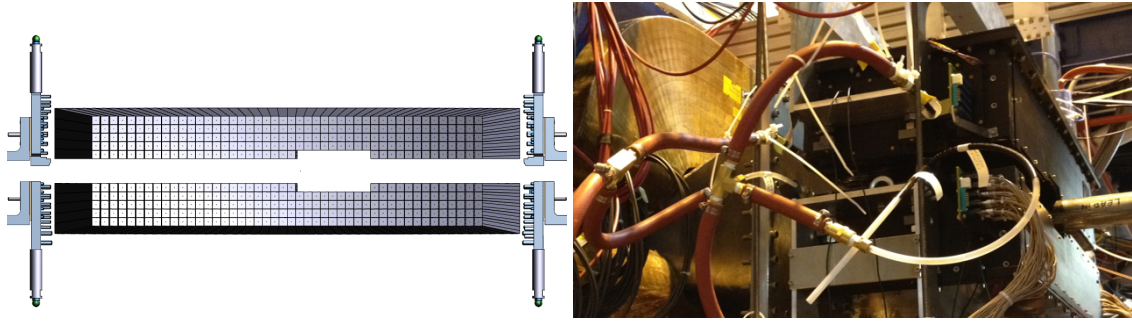


Figure 9: Rendered layout view (left) and the ECal assembly on the beam line (right).



Figure 10: The JLab FADC250 VXS module.

ECal. In the Test run 385 out of 442 modules (87%) was used in offline reconstruction, 39 modules were disabled or not read out (no FADC channel available, no APD bias voltage or masked out due to excessive noise) and 18 was masked offline due to noise.

6. Trigger and Data Acquisition

The DAQ system handles acquisition of data from the ECal and SVT sub-detectors with two DAQ architectures. The SVT DAQ is based on Advanced Telecom Communications Architecture (ATCA) hardware while the ECal uses VXS based hardware. Data from the sub-detectors are only readout when a trigger signal from the trigger system is received formed on input from the ECal.

6.1. Trigger system

The trigger system is designed to select time coincidences of electromagnetic clusters in the top and bot-

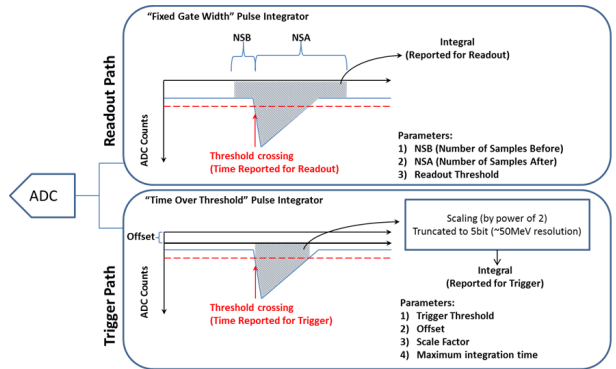


Figure 11: The two different readout modes of the FADC used in the Test run.

tom halves of the ECal. Figure 12 shows a schematic overview of each stage of the system. Each channel on the FADC board have an independent data path to send a 5-bit pulse energy and 3-bit pulse arrival time information to a trigger processing board (CTP) in the same crate every 32 ns. Contrary to the readout path described in Sec. 5.3, this energy is a pedestal subtracted time-over-threshold sum with programmable offsets and minimum threshold discriminator for each channel. With



Figure 12: Block diagram of the ECAL trigger system consisting of the FADC that samples and digitizes signals for each detector channel and sends them for cluster finding in the CTP. The CTP clusters are sent to the SSP where the final trigger decision is taken based on pairs of clusters in both halves of the ECal. The decision is sent to the Trigger Supervisor (TS) that generates the necessary signals to readout the sub-detectors.

input from all FADC channels, i.e. one half of the ECal, the CTP performs cluster finding and calculates cluster energy, shape and timing information. The 3x3 fixed-window, highly parallel, FPGA-based cluster algorithm simultaneously searches for up to 125 clusters with energy sum larger than the programmable energy threshold (in the Test run this was ≈ 270 MeV). Crystals in the fixed-window are included in the sum if the leading edges of the pulses occurred within a 8 ns time window (4 ns minimum). To take into account with clock skew and jitter throughout the system clustering algorithm can allow crystal hits from $N \in [0, 7]$ previous or future 4 ns clock cycles to contribute to the cluster sum. A separate sub-system board (SSP) receives the clusters (only the highest energy 3x3 window to deal with overlapping and very large clusters) from the top and bottom half CTP every 32 ns and searches for pairs of clusters in a 8 ns wide trigger window. The trigger supervisor (TS) generates all the necessary signals and controls the entire DAQ system readout through the trigger interface units installed in every crate that participate in the readout process.

The trigger system is free-running and driven by the 250 MHz global clock and has essentially zero dead time at the occupancies expected for HPS. The Trigger Supervisor can apply dead time if necessary, for example on a ‘busy’ or ‘full’ condition from the front-end electronics. The system is designed to handle trigger rates above 50 kHz and has a latency set to $\approx 3 \mu\text{s}$ to match that required by the SVT APV25 ASIC. During the Test run, for the most part the trigger system required only a single cluster in either the top or bottom Ecal halves and tested to above 100 kHz trigger rates with low thresholds.

6.2. SVT Data Acquisition

The SVT DAQ is based on the Reconfigurable Cluster Element (RCE) and cluster interconnect concept developed at SLAC as generic building blocks for DAQ systems. The RCE is a generic computational building block, housed on a separate daughter card called Data Processing Module (DPM), that are realized on an ATCA front board called the Cluster On Board (COB), see Fig. 13. The first generation RCE used in the Test run consisted of a Virtex 5 FPGA with 1 GB of DDR3 RAM. A schematic overview of the system is shown in Fig. 14. The analog outputs of up to 12 SVT half-modules (60 APV25 ASICs) are digitized on the Rear-Transition-Module (RTM), a custom board on the back side of the ATCA crate, interfacing the HPS readout to the generic DAQ components on the COB. A preamplifier converts the APV25 differential current out-



Figure 13: The SVT DAQ COB board with four data processing daughter cards visible on the left side.



Figure 14: Block diagram overview of the SVT DAQ.

put to a different voltage output scaled to the sensitive range of a 14-bit ADC operating at the system clock of 41.667 MHz. The RTM is organized into four sections with each section supporting three SVT half-module hybrids (15 APV25 ASICs). The RTM also includes a 4-channel fiber optic module and supporting logic which is used to interface to the JLab trigger system supervisor. Each section of the RTM is input to a DPM which applies thresholds for data reduction and organizes the sample data into UDP datagrams. The DPM also hosts an I²C controller used to configure and monitor the APV25 ASICs. A single ATCA crate with two COB cards was used, one supporting four DPMs and one supporting 3 DPMs and one DPM that is configured as the trigger and data transmission module. The two COB cards and their DPMs are interconnected with a 10Gb/s switch card [13] which also hosts two 1Gb/s Ethernet interfaces to the external SVT DAQ PC.

The external PC supports three network interfaces; two standard 1Gb/s Ethernet and one custom low latency data reception card. The first is used for slow control and monitoring of the 8 DPM modules and the second serves as the interface to the JLAB data acquisition system. The third custom low latency network interface is used to receive data from the ATCA crate and supports a low latency, reliable TTL trigger acknowledge

interface to the trigger DPM. This PC hosts the SVT control and monitoring software as well as the Read Out Controller application used to interface with the JLab DAQ.

While trigger rates during the Test run was significantly lower this system was tested at trigger rates up to 20 kHz and 50 MB/s.

6.3. General Data Acquisition and Online Computing

Every crate participating in the readout process contains a Readout Controller (ROC) that collects digitized information, processes it, and sends it on to the event builder. For the ECal, both VXS crates run ROC applications in a single blade Intel-based CPU module running under CentOS Linux OS. For the SVT DAQ, the ROC application runs on the external PC under RHEL. The event builder assembles information from the ROCs into a single event which is passed to the event recorder that writes it to a RAID5-based data storage system capable of handling up to 100 MB/s. The event builder and other critical components run on multicore Intel-based multi-CPU servers. The DAQ network system is a network router providing 10Gbit/s high-speed connection to the JLab computing facility for long-term storage. For the Test run, both the SVT and ECal ROC had a 1Gbit/s link to the network router.

7. Performance

7.1. SVT Performance

For the duration of the Test run all SVT modules and APV25 chips were configured to their nominal operating points [16] with all sensors reverse-biased at 180 V. The sensors were operated within a temperature range of 20 – 24°C. Approximately 97% of the 12,780 SVT channels were found to be operating normally; the fraction of dead or noisy channels varied from 2.4% to 4.7% throughout the Test run. Most of these were due to 2–4 misconfigured APV25 ASICs, a known noisy half-module and a couple of known APV25 ASICs.

7.1.1. Cluster and Hit Reconstruction

After a trigger is received, six samples of the corresponding output of the APV25 ASIC shaper circuit are digitized. The six pedestal-subtracted samples from every channel in the SVT are the basis for offline hit reconstruction. The typical pulse shape obtained shown in Fig. 15 also demonstrates that the SVT was well timed in to the trigger with the rise of the pulse at the 3rd sampling point. These hits are passed through a simple clustering algorithm which forms clusters by grouping

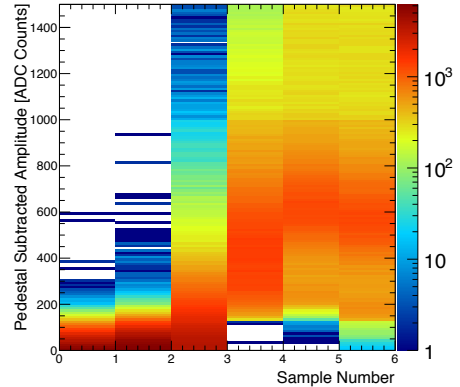


Figure 15: Accumulation of six pedestal-subtracted samples from individual SVT channels associated with hits on tracks.

adjacent strips with the position of a cluster on the sensor determined by the amplitude-weighted mean. With a linear gain up to ≈ 3 MIPs, the cluster charge for hits associated with a track follow the characteristic Landau shape, see Fig. 16. A noise level between $1.1 - 1.5 \times 10^3$ electrons was established through multiple calibration runs giving a signal to noise ratio of 21 – 25. Lab-based radioactive source tests was used to provide the absolute charge normalization.

In order to find the time and amplitude of each hit, t_0 , the six samples from each channel are fitted to an ideal $CR - RC$ function. After clustering hits on a sensor, the hit time for each cluster is computed as the amplitude-weighted average of the individually fitted t_0 on each channel. The t_0 -resolution is studied by comparing the cluster hit time with the average of all cluster hit times on the track, see Fig. 17, which has the expected jitter due to clock phase and trigger, approximately 25 ns. After correcting for offsets from each sensor (time-of-flight, clock phase) and accounting for the correlation between the t_0 and track time, the extracted t_0 resolution is 2.6 ns. This is somewhat worse than the approximately 2 ns resolution expected for S/N 25 which we attribute to the true pulse shape differing from our idealized fit function which will be improved in the future. Reducing the APV25 ASIC pulse shaping time will also improve time resolution. These results show that we can operate with the six sample readout mode of the APV25 chip and achieve time resolution adequate for pileup rejection during electron running in HPS.

While occupancy was slightly larger than expected, good agreement between data and simulation was found after taking into account dead or noisy channels. The hit

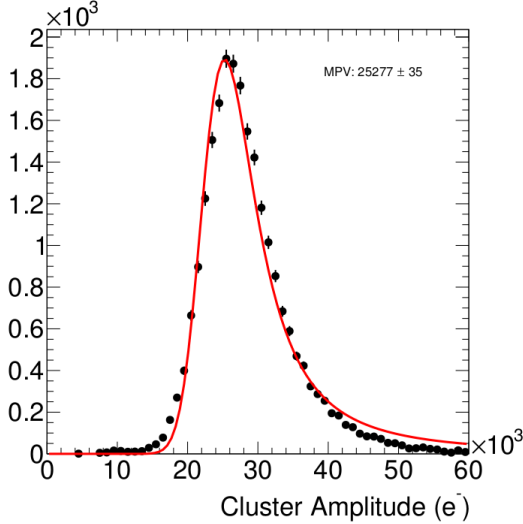


Figure 16: The cluster charge distribution for hits associated with a track.

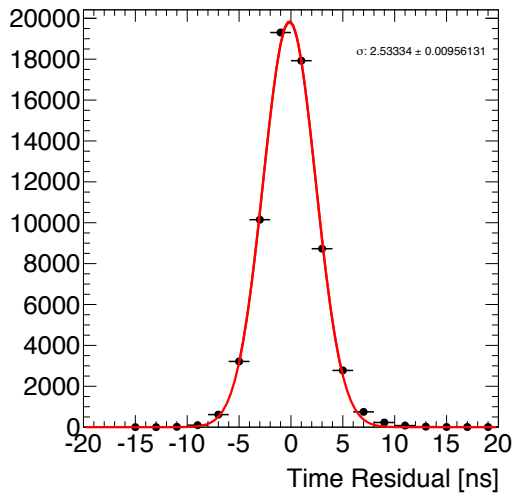


Figure 17: The residual of individual cluster times with the average of all clusters on the track.

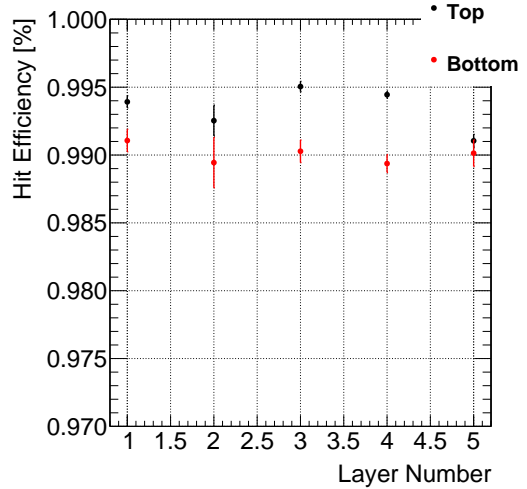


Figure 18: The hit reconstruction efficiency as a function of detector layer.

efficiency was estimated by measuring the number of good tracks with a hit close to the extrapolated intersection of a given sensor that was excluded from the track fit itself. Tracks which intersect regions with known bad channels or very close to in the edge region are excluded. The hit efficiency, see Fig. 18, was measured to be above 98% and fairly uniform across the SVT. The spatial resolution of similar microstrip sensors is well established by test beam data, against which the charge deposition model in the simulation is validated. This resolution can be parameterized as a function of the total signal to single-strip noise and the crossing angle of tracks through the sensor. The single-hit resolution for charged particles with signal to noise ratio above 20, as demonstrated here, is relatively constant at approximately $6 \mu\text{m}$ for tracks that enter approximately normal to the sensors as in HPS.

7.1.2. Momentum and Vertexing Resolution

By selecting e^+e^- pairs from the triggered events we are able to study basic distributions of pair production kinematics. Pairs of opposite charge tracks, one in the top and one in the bottom half of the SVT, with momentum larger than 400 MeV were selected. The pair production kinematics are relatively well reproduced given the alignment of the tracker as shown in Fig. 19.

The expected momentum resolution from simulation is between 4-5% for tracks in the momentum range of the

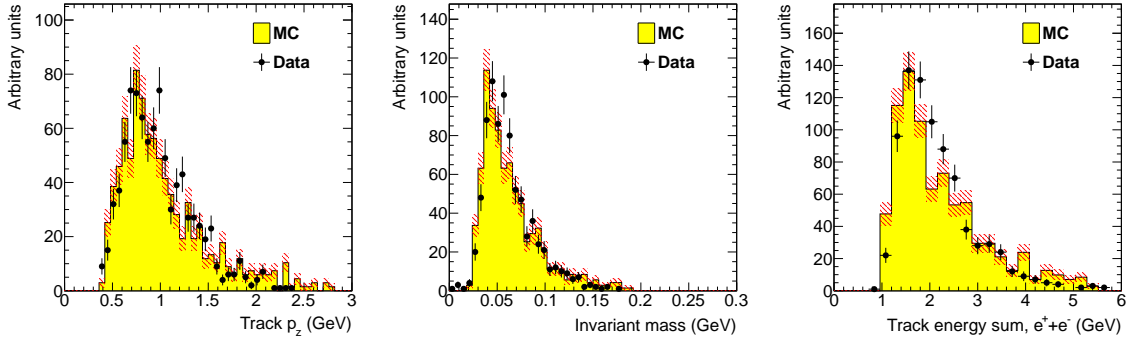


Figure 19: Kinematic distributions for e^+e^- pairs selected by opposite charged tracks in the top and bottom half of the tracker: track momentum in the top half of the SVT (left), invariant mass (middle) and the sum of the track momentum for the pair (right).

Test run. This is significantly smaller than the accuracy at which we're able estimate the scale and resolution in the Test run. By looking at the agreement between data and simulation in the shape of the kinematic distributions for single- and two track events and adjusting the overall momentum scale and smearing simulated events with a Gaussian resolution we estimate an uncertainty of 10% on both the momentum scale and resolution.

For the vertexing performance the foremost difference compared to electron beam running is that the target was located approximately 67 cm upstream from our nominal target position; giving almost collinear tracks in the detector. This degrades the vertex resolution along the beam line compared to that expected in an electron beam with nominal target position. Furthermore, tails of the vertex distributions are impossible to study with the finite data sample obtained in the Test run. Nevertheless, useful information can still be obtained by studying the vertex distributions. Figure 20 shows the distance of closest approach of the momentum vectors extrapolated in the upstream direction from our analyzing magnet, taking into account the measured fringe field of the PS dipole magnet.

7.2. ECal Performance

The integrated pulse of the each channel was converted to energy by first subtracting the pedestal and then applying a conversion factor to convert ADC counts to energy. The pedestals are measured using special runs where each trigger records 100 samples of signals from the APDs with 4 ns between each sample. The pedestals were extracted from the part of the window before the actual hit in the calorimeter. After subtracting the pedestal, modules with integrated pulse above a

threshold are clustered using a simple algorithm similar to the one deployed for the trigger (see Sec. 6.1). Due to the high effective readout threshold of 73 MeV the average number of modules in a cluster was ~ 3 and the simple clustering algorithm worked well for reconstruction of the detected shower energy. An average noise level of approximately 15 MeV was measured in special pedestal runs.

The ratio of the ECal cluster energy E to the momentum p of a matched track in the SVT was used to determine the conversion factors from ADC counts to energy. To compare data and simulation, all inoperable or noisy channels in the SVT and ECal was disabled in both data and simulation; any efficiency or bias that affect the data should be reflected in the simulation. representing the average E/p for clusters that include the crystal Iteratively, conversion coefficients for each module is adjusted until the E/p ratio in data and simulation are similar. The distribution of the E/p ratio in data and simulation can be seen in Fig. 21. The peak position of the distribution indicates the sampling fraction of the ECal, the fraction of the incident particle energy measured in the cluster. The width and tails of the distribution in data indicates imperfect calibration and noise of the ECal modules. This level of calibration and the agreement with simulation was found to be sufficient for the multiple scattering analysis using normalized event rates described in Sec. 8.

7.3. Trigger Performance

The trigger and DAQ integrate pulses from the ECal modules differently to measure the energy deposited in the each crystal. The trigger integrates the pulse using a time-over-threshold window, and the DAQ readout integrates using a fixed-size window (5 samples before and 30 samples after a threshold crossing). For every

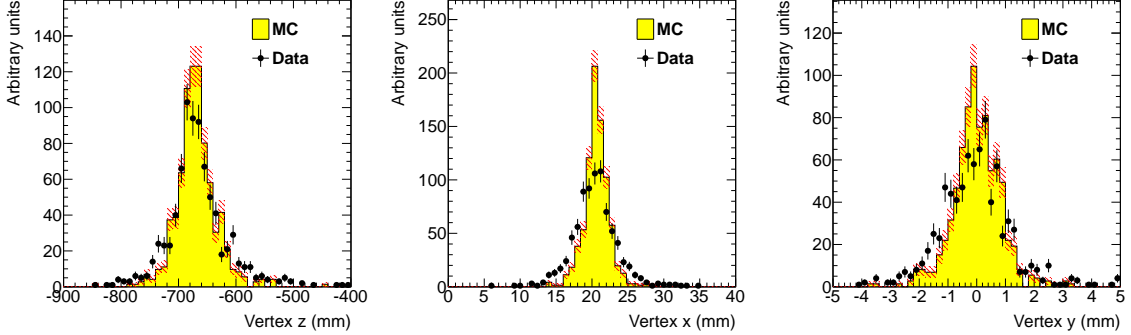


Figure 20: Vertex position represented by the distance of closest approach of the extrapolated momentum vectors upstream of the PS dipole magnet taking into account the measured fringe field. The overall shift from zero in the x-direction is due to a 30 mrad rotation of the SVT with respect to the beam line.

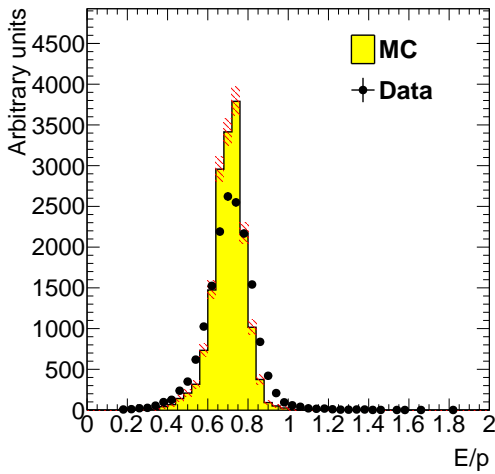


Figure 21: The ECal energy over track momentum ratio comparing data and simulation

event, the trigger reports the trigger decision as a bit mask (top half, bottom half or both) and the time the trigger fired. The trigger performance was studied by simulating the trigger for each event and comparing to how the events were actually triggered. First, we simulate the FADC readout board to convert from readout hits (with fixed-size window integration) to trigger hits (time-over-threshold integration). Secondly, the CTP clustering algorithm and the trigger decision is simulated before we compare the trigger decision and trigger time to what was reported by the actual trigger. To eliminate trigger bias, we use a tag and probe method. To study the trigger performance in one half of the ECal, we select events which triggered the other half and where there was exactly one probe cluster in the ECal half under study. We then measure trigger efficiency as the fraction of tagged events that fired the trigger in the probe half as a function of the probe cluster energy, shown in Fig. 22. As a cross-check, the turn-on from the trigger threshold was measured to be 1280 in units of ADC counts as expected. The threshold was not perfectly sharp because of uncertainties in the conversion from readout to trigger hits described above, but based on comparisons with simulation we found that the trigger worked exactly as specified. The trigger turn-on is slow and reaches an uneven plateau just below 1 GeV for two reasons; gain variations between different crystals lead to the threshold variations and the nonlinearity of the time-over-threshold integral means that the effective threshold is higher for clusters that span multiple crystals. The effective trigger threshold is therefore dependent on position and energy of the particle as well as cluster multiplicity.

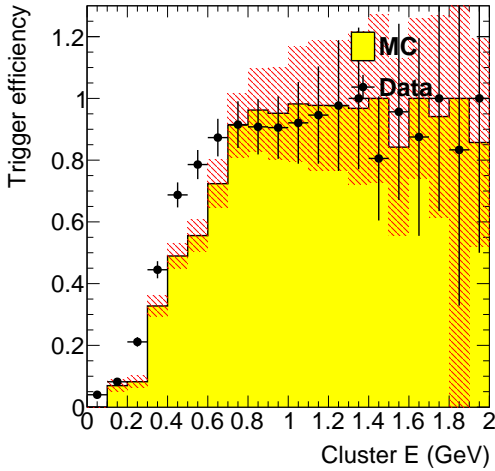


Figure 22: Trigger efficiency in both halves of the ECal for data and simulation as a function of cluster energy.

8. Multiple Coulomb Scattering Distributions

Occupancies close to the beam create many of the key challenges in the HPS experiment and determine the limits of sensitivity to low A' masses. These occupancies are dominated by electrons which have multiple Coulomb scattered (MCS) to relatively large angles in the target. Because HPS is sensitive to scattering angles far out on the tail of the MCS distribution, well beyond the angles important in other experiments, care must be taken to ensure our simulations are correct in this regime.

8.1. Multiple Coulomb Scattering Models

One of the main goals of the HPS Test was to evaluate the description of the tails of the MCS to gain further confidence in the expected detector occupancy in the full HPS experiment. Previous studies of multiple scattering angles show good agreement with the Molière theory [17] for a wide range of materials and projectiles [18, 19, 20]. We have verified that the angular distribution $F(\theta)$ in the differential cross section $d\sigma = F(\theta)d(\cos\theta)d\phi$ for the EGS5 [21] simulation program show good agreement with Molière's analytical formula as formulated by Bethe [22]. The small angle approximation was also shown to be in agreement with the theory formulated by Gaudsmits and Saunderson [23, 24] that is valid for any angle. While EGS5 uses the more complex and time consuming Molière formula, the default physics list of GEANT4 uses the so-called Urban model, an approximation with two, con-

Converter thickness (% X_0)	Duration (s)	e^- on converter (μC)
1.6	911	24.4
0.18	2640	193.5
0.45	2149	140.7
0	1279	88.1

Table 3: Measured integrated currents for the dedicated photon runs.

tinuously joined, functions to take into account small and large angle scattering. Due to the explicit function in large angle approximation used by GEANT4 we expect that GEANT4 will overestimate the angular distribution at angles larger than a few mrad.

Figure 3 gives a schematic view of the main differences between the photon and electron beam setup. The angular distribution of the pair produced electron and positron emerging from the converter in the test run has comparable contributions from *i*) the pair production angle and *ii*) the MCS of the electron and positron in the converter after production. By measuring the scattering rate at several different converter thicknesses we can vary the contribution from MCS while the contribution from the pair production angle is constant. This allows us to confirm our model of MCS despite the fact that all data was taken with a photon beam.

8.2. Running Conditions

Data was taken at three different converter thicknesses with a beam current varying between 30 – 70 nA, see Tab. 3. The photon beam line during the test run produced a relatively large fraction of pairs originating upstream of the converter. This contribution was measured during data taking with “empty” converter runs i.e. removing the converter but with all other conditions the same. The upstream background measured in the “empty” converter runs was subtracted from the other runs, properly normalized using the measured integrated currents.

8.3. Measured Angular Distributions

For this analysis, we measure angular distribution of electrons and positrons using the ECal. Cluster reconstruction was done using the algorithm described in Sec. 6.1 build clusters around seed hits (hits above a “seed” energy threshold and with greater energy than any neighboring hits), and add all neighboring hits above an “add” energy threshold. Hit energy is calibrated by matching track momentum to cluster energy, as described in Sec. 7.2. The measured angular distribution in the ECal for the three converter thicknesses

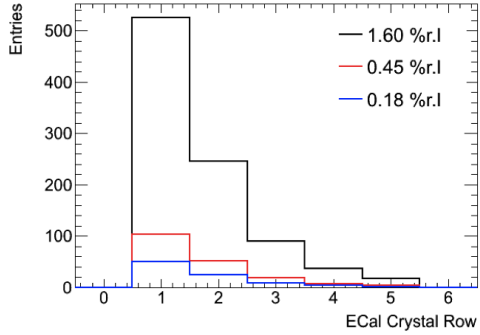


Figure 23: Measured vertical angular distributions after integrated beam current normalization and background subtraction.

are shown in Fig. 23. The data has been normalized to the integrated beam current and the background has been subtracted. The background fraction for the three converter thicknesses was 16%, 52% and 71% for converter thicknesses of 1.6%, 0.45% and 0.18%, respectively. The background fraction was also cross-checked by pointing back tracks reconstructed in the SVT to identify the fraction of tracks not emanating from the converter. We also checked that the contribution from photons to our triggered sample was less than 2% (without angular selections which would further reduce the contribution).

These measured angular distributions are compared to simulation to validate the modeling of the MCS. EGS5 [21] is used to generate the electromagnetic interactions in the converter while GEANT4 is used to simulate the particles after the converter. Figure 24 shows the angular distribution comparing data and EGS5 normalized to 1 s of beam at 90 nA beam current with a converter thickness of 1.6%. Reasonable agreement is obtained in the most important region close to the beam. There is a hint of a slightly different slope of the data at larger angles; this difference is covered by systematic uncertainties. The total rates for each converter thickness is shown in Fig. 25 and summarized in Tab. 8.3.

The total systematic uncertainty was estimated to be between 10-18% depending on the run including: a 5% uncertainty on the integrated current normalization, alignment of the ECal, uncertainty from the background normalization, and limited Monte Carlo statistics.

8.4. Conclusion

In summary, the accurate modeling of the MCS is fundamental to estimate occupancies and trigger rates

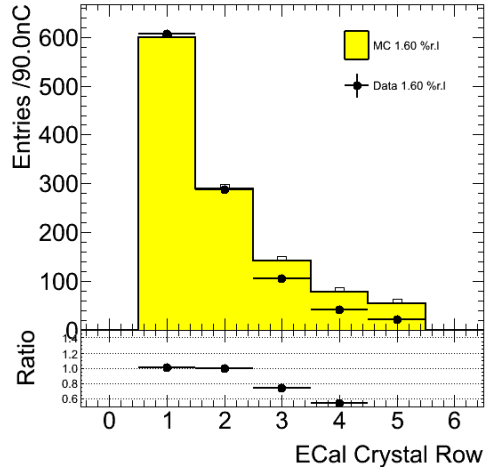


Figure 24: Comparison between the observed and predicted angular distribution using EGS5 for a converter thickness of 1.6%. Similar agreement is found for 0.45% and 0.18% converter thicknesses. Only statistical uncertainties are shown.

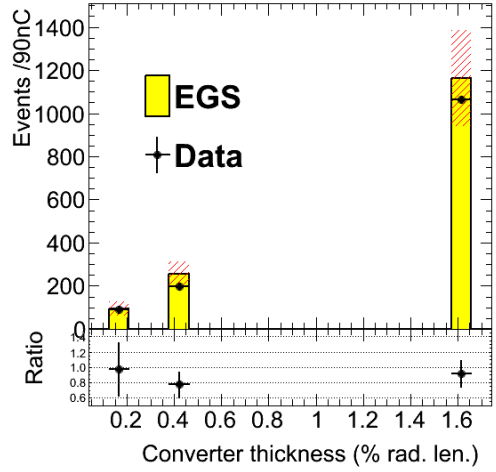


Figure 25: The measured rate as a function of converter thickness for data and EGS5 simulation of MCS in the converter.

Converter (% r.l.)	1.60	0.45	0.18
EGS5	1162 ± 112	255 ± 28	94 ± 17
GEANT4	2633 ± 250	371 ± 38	114 ± 18
Observed	1064 ± 2	196 ± 1	92 ± 1

Table 4: Observed and predicted number of events for 1 s of beam at 90 nA for three different converter thicknesses. The uncertainty on the prediction includes systematic uncertainties.

for HPS. EGS5 predicts the correct angular distribution across all converter thicknesses as expected while Geant4, using the so-called Urban model for multiple scattering overestimates the rates; with the disagreement increasing with larger converter thickness. This preliminary result verifies similar studies [] and gives confidence in our modeling of the MCS using EGS5 for evaluating the physics reach of HPS.

9. Summary and Outlook

The HPS Test Run experiment, using a simplified version of the apparatus planned for the full HPS experiment in a parasitic photon beam, demonstrated the feasibility of the detector technologies proposed for the HPS silicon tracker, ECal, and data acquisition systems. Performance from each of these subsystems has been shown to be adequate to conduct the full experiment successfully. A measurement of the normalized trigger rates from a photon conversion target confirmed expectations from simulation, giving credence to estimates of the trigger rates and the detector backgrounds expected in electron beam running.

10. Acknowledgements

References

- [1] B. Holdom, Two U(1)'s and Epsilon Charge Shifts, *Phys.Lett.* B166 (1986) 196.
- [2] N. Arkani-Hamed, D. P. Finkbeiner, T. R. Slatyer, N. Weiner, A Theory of Dark Matter, *Phys.Rev.* D79 (2009) 015014.
- [3] J. D. Bjorken, R. Essig, P. Schuster, N. Toro, New Fixed-Target Experiments to Search for Dark Gauge Forces, *Phys.Rev.* D80 (2009) 075018.
- [4] A. G. *et al.* (HPS Collaboration), HPS Heavy Photon Search Proposal, 2010.
- [5] A. Sandorfi, *et al.*, 2012. URL: http://www.jlab.org/exp_prog/proposals/06/PR-06-101.pdf.
- [6] A. G. *et al.* (HPS Collaboration), HPS Test Run Proposal to DOE, 2011.
- [7] I. Rashevskaya, S. Bettarini, G. Rizzo, L. Bosisio, S. Dittongo, *et al.*, Radiation damage of silicon structures with electrons of 900-MeV, *Nucl.Instrum.Meth.* A485 (2002) 126–132.
- [8] S. A. *et al.*, Geant4a simulation toolkit, *Nucl.Instrum.Meth.* A506 (2003) 250 – 303.
- [9] N. A. Graf, org.lcsim: Event reconstruction in Java, *J.Phys.Conf.Ser.* 331 (2011) 032012.
- [10] D. S. Denisov, S. Soldner-Rembold, DO Run IIB Silicon Detector Upgrade: Technical Design Report (2001).
- [11] M. French, L. Jones, Q. Morrissey, A. Neviani, R. Turchetta, *et al.*, Design and results from the APV25, a deep sub-micron CMOS front-end chip for the CMS tracker, *Nucl.Instrum.Meth.* A466 (2001) 359–365.
- [12] M. Friedl, C. Irmler, M. Pernicka, Readout of silicon strip detectors with position and timing information, *Nucl.Instrum.Meth.* A598 (2009) 82–83.
- [13] R. Larsen, Emerging New Electronics Standards for Physics, *Conf.Proc.* C110904 (2011) 1981–1985.
- [14] A. Radyushkin, P. Stoler (Eds.), Inner Calorimeter in Clas/dvcs Experiment, 2008.
- [15] D. H., *et al.*, Integrated tests of a high speed VX5 switch card and 250 MSPS flash ADCs, 2007. doi:10.1109/NSSMIC.2007.4436457.
- [16] L. Jones, APV25-S1: User guide version 2.2, RAL Microelectronics Design Group, 2011.
- [17] G. Moliere, Theory of the scattering of fast charged particles. 2. Repeated and multiple scattering, *Z.Naturforsch.* A3 (1948) 78–97.
- [18] D. Attwood, P. Bell, S. Bull, T. McMahon, J. Wilson, *et al.*, The scattering of muons in low Z materials, *Nucl.Instrum.Meth.* B251 (2006) 41–55.
- [19] G. Shen, C. Ankenbrandt, M. Atac, R. M. Brown, S. Ecklund, *et al.*, Measurement of Multiple Scattering at 50-GeV/c to 200-GeV/c, *Phys.Rev.* D20 (1979) 1584.
- [20] B. Gottschalk, A. Koehler, R. Schneider, J. Sisterson, M. Wagner, Multiple coulomb scattering of 160 mev protons, *Nuclear Instruments and Methods in Physics Research Section B: Beam Interactions with Materials and Atoms* 74 (1993) 467 – 490.
- [21] H. Hirayama, Y. Namito, A. Bielajew, S. Wilderman, W. Nelson, The EGS5 Code System, 2005.
- [22] H. Bethe, Moliere's theory of multiple scattering, *Phys.Rev.* 89 (1953) 1256–1266.
- [23] S. Goudsmit, J. Saunderson, Multiple Scattering of Electrons, *Phys.Rev.* 57 (1940) 24–29.
- [24] S. Goudsmit, J. Saunderson, Multiple Scattering of Electrons. II, *Phys.Rev.* 58 (1940) 36–42.